Cross section for forward J/ψ production in $p\bar{p}$ collisions at $\sqrt{s}=1.8$ TeV

D. Acosta,[1] T. Affolder,[2] H. Akimoto,[3] M. G. Albrow,[4] D. Ambrose,[5] D. Amidei,[6] K. Anikeev,[7] J. Antos,[8] G. Apollinari,[4] T. Arisawa,[3] A. Artikov,[9] T. Asakawa,[10] W. Ashmanskas,[11] F. Azfar,[12] P. Azzi-Bacchetta,[13] N. Bacchetta,[13] H. Bachacou,[2] W. Badgett,[4] S. Bailey,[14] P. de Barbaro,[15] A. Barbaro-Galtieri,[2] V. E. Barnes,[16] B. A. Barnett,[17] S. Baroiant,[18] M. Barone,[19] G. Bauer,[7] F. Bedeschi,[20] S. Behari,[17] S. Belforte,[21] W. H. Bell,[22] G. Bellettini,[20] J. Bellinger,[23] D. Benjamin,[24] J. Bensinger,[25] A. Beretvas,[4] J. Berryhill,[11] A. Bhatti,[26] M. Binkley,[4] D. Bisello,[13] M. Bishai,[4] R. E. Blair,[27] C. Blocker,[25] K. Bloom,[6] B. Blumenfeld,[17] S. R. Blusk,[15] A. Bocci,[26] A. Bodek,[15] G. Bolla,[16] A. Bolshov,[7] Y. Bonushkin,[28] D. Bortoletto,[16] J. Boudreau,[29] A. Brandl,[30] C. Bromberg,[31] M. Brozovic,[24] E. Brubaker,[2] N. Bruner,[30] J. Budagov,[9] H. S. Budd,[15] K. Burkett,[14] G. Busetto,[13] K. L. Byrum,[27] S. Cabrera,[24] P. Calafiura,[2] M. Campbell,[6] W. Carithers,[2] J. Carlson,[6] D. Carlsmith,[23] W. Caskey,[18] A. Castro,[32] D. Cauz,[21] A. Cerri,[20] L. Cerrito,[33] A. W. Chan,[8] P. S. Chang,[8] P. T. Chang,[8] J. Chapman,[6] C. Chen,[5] Y. C. Chen,[8] M.-T. Cheng,[8] M. Chertok,[18] G. Chiarelli,[20] I. Chirikov-Zorin,[9] G. Chlachidze,[9] F. Chlebana,[4] L. Christofek,[33] M. L. Chu,[8] J. Y. Chung,[34] W.-H. Chung,[23] Y. S. Chung,[15] C. I. Ciobanu,[34] A. G. Clark,[35] M. Coca,[20] A. P. Colijn,[4] A. Connolly,[2] M. Convery,[26] J. Conway,[36] M. Cordelli,[19] J. Cranshaw,[37] R. Culbertson,[4] D. Dagenhart,[25] S. D'Auria,[22] F. DeJongh,[4] S. Dell'Agnello,[19] M. Dell'Orso,[20] S. Demers,[15] L. Demortier,[26] M. Deninno,[32] P. F. Derwent,[4] T. Devlin,[36] J. R. Dittmann,[4] A. Dominguez,[2] S. Donati,[20] M. D'Onofrio,[20] T. Dorigo,[13] I. Dunietz,[4] N. Eddy,[33] K. Einsweiler,[2] E. Engels Jr.,[29] R. Erbacher,[4] D. Errede,[33] S. Errede,[33] Q. Fan,[15] H.-C. Fang,[2] S. Farrington,[22] R. G. Feild,[38] J. P. Fernandez,[16] C. Ferretti,[20] R. D. Field,[1] I. Fiori,[32] B. Flaugher,[4] L. R. Flores-Castillo,[29] G. W. Foster,[4] M. Franklin,[14] J. Freeman,[4] J. Friedman,[7] Y. Fukui,[39] I. Furic,[7] S. Galeotti,[20] A. Gallas,[40] M. Gallinaro,[26] T. Gao,[5] M. Garcia-Sciveres,[2] A. F. Garfinkel,[16] P. Gatti,[13] C. Gay,[38] D. W. Gerdes,[6] E. Gerstein,[41] P. Giannetti,[20] K. Giolo,[16] M. Giordani,[18] P. Giromini,[19] V. Glagolev,[9] D. Glenzinski,[4] M. Gold,[30] J. Goldstein,[4] G. Gomez,[42] M. Goncharov,[43] I. Gorelov,[30] A. T. Goshaw,[24] Y. Gotra,[29] K. Goulianos,[26] C. Green,[16] A. Gresele,[13] G. Grim,[18] C. Grosso-Pilcher,[11] M. Guenther,[16] G. Guillian,[6] J. Guimaraes da Costa,[14] R. M. Haas,[1] C. Haber,[2] S. R. Hahn,[4] E. Halkiadakis,[15] C. Hall,[14] T. Handa,[44] R. Handler,[23] F. Happacher,[19] K. Hara,[10] A. D. Hardman,[16] R. M. Harris,[4] F. Hartmann,[45] K. Hatakeyama,[26] J. Hauser,[28] J. Heinrich,[5] A. Heiss,[45] M. Hennecke,[45] M. Herndon,[17] C. Hill,[46] A. Hocker,[15] K. D. Hoffman,[11] R. Hollebeek,[5] L. Holloway,[33] B. T. Huffman,[12] R. Hughes,[34] J. Huston,[31] J. Huth,[14] H. Ikeda,[10] J. Incandela,[46] G. Introzzi,[20] A. Ivanov,[15] J. Iwai,[3] Y. Iwata,[44] B. Iyutin,[7] E. James,[6] M. Jones,[5] U. Joshi,[4] H. Kambara,[35] T. Kamon,[43] T. Kaneko,[10] M. Karagoz Unel,[40] K. Karr,[47] S. Kartal,[4] H. Kasha,[38] Y. Kato,[48] T. A. Keaffaber,[16] K. Kelley,[7] M. Kelly,[6] R. D. Kennedy,[4] R. Kephart,[4] D. Khazins,[24] T. Kikuchi,[10] B. Kilminster,[15] B. J. Kim,[49] D. H. Kim,[49] H. S. Kim,[33] M. J. Kim,[41] S. B. Kim,[49] S. H. Kim,[10] T. H. Kim,[7] Y. K. Kim,[2] M. Kirby,[24] M. Kirk,[25] L. Kirsch,[25] S. Klimenko,[1] P. Koehn,[34] K. Kondo,[3] J. Konigsberg,[1] A. Korn,[7] A. Korytov,[1] K. Kotelnikov,[50] E. Kovacs,[27] J. Kroll,[5] M. Kruse,[24] V. Krutelyov,[43] S. E. Kuhlmann,[27] K. Kurino,[44] T. Kuwabara,[10] A. T. Laasanen,[16] N. Lai,[11] S. Lami,[26] S. Lammel,[4] J. Lancaster,[24] K. Lannon,[33] M. Lancaster,[51] R. Lander,[18] A. Lath,[36] G. Latino,[30] T. LeCompte,[27] Y. Le,[17] K. Lee,[37] S. W. Lee,[43] N. Leonardo,[7] S. Leone,[20] J. D. Lewis,[4] M. Lindgren,[28] T. M. Liss,[33] J. B. Liu,[15] T. Liu,[4] Y. C. Liu,[8] D. O. Litvintsev,[4] O. Lobban,[37] N. S. Lockyer,[5] A. Loginov,[50] J. Loken,[12] M. Loreti,[13] D. Lucchesi,[13] P. Lukens,[4] S. Lusin,[23] L. Lyons,[12] J. Lys,[2] R. Madrak,[14] K. Maeshima,[4] P. Maksimovic,[17] L. Malferrari,[32] M. Mangano,[20] G. Manca,[12] M. Mariotti,[13] G. Martignon,[13] M. Martin,[17] A. Martin,[38] V. Martin,[40] J. A. J. Matthews,[30] P. Mazzanti,[32] K. S. McFarland,[15] P. McIntyre,[43] M. Menguzzato,[13] A. Menzione,[20] P. Merkel,[4] C. Mesropian,[26] A. Meyer,[4] T. Miao,[4] R. Miller,[31] J. S. Miller,[6] H. Minato,[10] S. Miscetti,[19] M. Mishina,[39] G. Mitselmakher,[1] Y. Miyazaki,[48] N. Moggi,[32] E. Moore,[30] R. Moore,[6] Y. Morita,[39] T. Moulik,[16] M. Mulhearn,[7] A. Mukherjee,[4] T. Muller,[45] A. Munar,[20] P. Murat,[4] S. Murgia,[31] J. Nachtman,[28] V. Nagaslaev,[37] S. Nahn,[38] H. Nakada,[10] I. Nakano,[44] R. Napora,[17] C. Nelson,[4] T. Nelson,[4] C. Neu,[34] M. S. Neubauer,[7] D. Neuberger,[45] C. Newman-Holmes,[4] C.-Y. P. Ngan,[7] T. Nigmanov,[29] H. Niu,[25] L. Nodulman,[27] A. Nomerotski,[1] S. H. Oh,[24] Y. D. Oh,[49] T. Ohmoto,[44] T. Ohsugi,[44] R. Oishi,[10] T. Okusawa,[48] J. Olsen,[23] W. Orejudos,[2] C. Pagliarone,[20] F. Palmonari,[20] R. Paoletti,[20] V. Papadimitriou,[37] D. Partos,[25] J. Patrick,[4] G. Pauletta,[21] M. Paulini,[41] T. Pauly,[12] C. Paus,[7] D. Pellett,[18] A. Penzo,[21] L. Pescara,[13] T. J. Phillips,[24] G. Piacentino,[20] J. Piedra,[42] K. T. Pitts,[33] A. Pompos,[16] L. Pondrom,[23] G. Pope,[29] T. Pratt,[12] F. Prokoshin,[9] J. Proudfoot,[27] F. Ptohos,[19] O. Pukhov,[9] G. Punzi,[20] J. Rademacker,[12] A. Rakitine,[7] F. Ratnikov,[37] D. Reher,[2] A. Reichold,[12] P. Renton,[12] A. Ribon,[13] W. Riegler,[14] F. Rimondi,[32] L. Ristori,[20] M. Riveline,[52] W. J. Robertson,[24] T. Rodrigo,[42] S. Rolli,[47] L. Rosenson,[7] R. Roser,[4] R. Rossin,[13] C. Rott,[16] A. Roy,[16] A. Ruiz,[42] D. Ryan,[47] A. Safonov,[18] R. St. Denis,[22] W. K. Sakumoto,[15] D. Saltzberg,[28] C. Sanchez,[34] A. Sansoni,[19] L. Santi,[21] H. Sato,[10] P. Savard,[52] A. Savoy-Navarro,[4] P. Schlabach,[4] E. E. Schmidt,[4] M. P. Schmidt,[38] M. Schmitt,[40] L. Scodellaro,[13] A. Scott,[28] A. Scribano,[20] A. Sedov,[16] S. Seidel,[30] Y. Seiya,[10] A. Semenov,[9] F. Semeria,[32] T. Shah,[7] M. D. Shapiro,[2] P. F. Shepard,[29] T. Shibayama,[10] M. Shimojima,[10] M. Shochet,[11] A. Sidoti,[13] J. Siegrist,[2] A. Sill,[37] P. Sinervo,[52] P. Singh,[33] A. J. Slaughter,[38] K. Sliwa,[47] F. D. Snider,[4] R. Snihur,[51] A. Solodsky,[26] J. Spalding,[4] T. Speer,[35] M. Spezziga,[37] P. Sphicas,[7] F. Spinella,[20] M. Spiropulu,[11] L. Spiegel,[4] J. Steele,[23] A. Stefanini,[20] J. Strologas,[33] F. Strumia,[35] D. Stuart,[46] A. Sukhanov,[1] K. Sumorok,[7] T. Suzuki,[10] T. Takano,[12] R. Takashima,[44] K. Takikawa,[10] P. Tamburello,[24] M. Tanaka,[10] B. Tannenbaum,[28] M. Tecchio,[6] R. J. Tesarek,[4] P. K. Teng,[8] K. Terashi,[26] S. Tether,[7] A. S. Thompson,[22] E. Thomson,[34] R. Thurman-Keup,[27] P. Tipton,[15] S. Tkaczyk,[4] D. Toback,[43] K. Tollefson,[31] A. Tollestrup,[4] D. Tonelli,[20] M. Tonnesmann,[31] H. Toyoda,[48]

W. Trischuk,[52] J. F. de Troconiz,[14] J. Tseng,[7] D. Tsybychev,[1] N. Turini,[20] F. Ukegawa,[10] T. Unverhau,[22] T. Vaiciulis,[15] J. Valls,[36] E. Vataga,[20] S. Vejcik III,[4] G. Velev,[4] G. Veramendi,[2] R. Vidal,[4] I. Vila,[42] R. Vilar,[42] I. Volobouev,[2] M. von der Mey,[28] D. Vucinic,[7] R. G. Wagner,[27] R. L. Wagner,[4] W. Wagner,[45] N. B. Wallace,[36] Z. Wan,[36] C. Wang,[24] M. J. Wang,[8] S. M. Wang,[1] B. Ward,[22] S. Waschke,[22] T. Watanabe,[10] D. Waters,[51] T. Watts,[36] M. Weber,[2] H. Wenzel,[45] W. C. Wester III,[4] B. Whitehouse,[47] A. B. Wicklund,[27] E. Wicklund,[4] T. Wilkes,[18] H. H. Williams,[5] P. Wilson,[4] B. L. Winer,[34] D. Winn,[6] S. Wolbers,[4] D. Wolinski,[6] J. Wolinski,[31] S. Wolinski,[6] M. Wolter,[47] S. Worm,[36] X. Wu,[35] F. Würthwein,[7] J. Wyss,[20] U. K. Yang,[11] W. Yao,[2] G. P. Yeh,[4] P. Yeh,[8] K. Yi,[17] J. Yoh,[4] C. Yosef,[31] T. Yoshida,[48] I. Yu,[49] S. Yu,[5] Z. Yu,[38] J. C. Yun,[4] A. Zanetti,[21] F. Zetti,[2] and S. Zucchelli[32]

(CDF Collaboration)

[1]*University of Florida, Gainesville, Florida 32611*
[2]*Ernest Orlando Lawrence Berkeley National Laboratory, Berkeley, California 94720*
[3]*Waseda University, Tokyo 169, Japan*
[4]*Fermi National Accelerator Laboratory, Batavia, Illinois 60510*
[5]*University of Pennsylvania, Philadelphia, Pennsylvania 19104*
[6]*University of Michigan, Ann Arbor, Michigan 48109*
[7]*Massachusetts Institute of Technology, Cambridge, Massachusetts 02139*
[8]*Institute of Physics, Academia Sinica, Taipei, Taiwan 11529, Republic of China*
[9]*Joint Institute for Nuclear Research, RU-141980 Dubna, Russia*
[10]*University of Tsukuba, Tsukuba, Ibaraki 305, Japan*
[11]*Enrico Fermi Institute, University of Chicago, Chicago, Illinois 60637*
[12]*University of Oxford, Oxford OX1 3RH, United Kingdom*
[13]*Universita di Padova, Istituto Nazionale di Fisica Nucleare, Sezione di Padova, I-35131 Padova, Italy*
[14]*Harvard University, Cambridge, Massachusetts 02138*
[15]*University of Rochester, Rochester, New York 14627*
[16]*Purdue University, West Lafayette, Indiana 47907*
[17]*The Johns Hopkins University, Baltimore, Maryland 21218*
[18]*University of California at Davis, Davis, California 95616*
[19]*Laboratori Nazionali di Frascati, Istituto Nazionale di Fisica Nucleare, I-00044 Frascati, Italy*
[20]*Istituto Nazionale di Fisica Nucleare, University and Scuola Normale Superiore of Pisa, I-56100 Pisa, Italy*
[21]*Istituto Nazionale di Fisica Nucleare, University of Trieste/Udine, Italy*
[22]*Glasgow University, Glasgow G12 8QQ, United Kingdom*
[23]*University of Wisconsin, Madison, Wisconsin 53706*
[24]*Duke University, Durham, North Carolina 27708*
[25]*Brandeis University, Waltham, Massachusetts 02254*
[26]*Rockefeller University, New York, New York 10021*
[27]*Argonne National Laboratory, Argonne, Illinois 60439*
[28]*University of California at Los Angeles, Los Angeles, California 90024*
[29]*University of Pittsburgh, Pittsburgh, Pennsylvania 15260*
[30]*University of New Mexico, Albuquerque, New Mexico 87131*
[31]*Michigan State University, East Lansing, Michigan 48824*
[32]*Istituto Nazionale di Fisica Nucleare, University of Bologna, I-40127 Bologna, Italy*
[33]*University of Illinois, Urbana, Illinois 61801*
[34]*The Ohio State University, Columbus, Ohio 43210*
[35]*University of Geneva, CH-1211 Geneva 4, Switzerland*
[36]*Rutgers University, Piscataway, New Jersey 08855*
[37]*Texas Tech University, Lubbock, Texas 79409*
[38]*Yale University, New Haven, Connecticut 06520*
[39]*High Energy Accelerator Research Organization (KEK), Tsukuba, Ibaraki 305, Japan*
[40]*Northwestern University, Evanston, Illinois 60208*
[41]*Carnegie Mellon University, Pittsburgh, Pennsylvania 15218*
[42]*Instituto de Fisica de Cantabria, CSIC–University of Cantabria, 39005 Santander, Spain*
[43]*Texas A&M University, College Station, Texas 77843*
[44]*Hiroshima University, Higashi-Hiroshima 724, Japan*
[45]*Institut für Experimentelle Kernphysik, Universität Karlsruhe, 76128 Karlsruhe, Germany*
[46]*University of California at Santa Barbara, Santa Barbara, California 93106*
[47]*Tufts University, Medford, Massachusetts 02155*
[48]*Osaka City University, Osaka 588, Japan*
[49]*Center for High Energy Physics, Kyungpook National University, Taegu 702-701, Korea,*

Seoul National University, Seoul 151-742, Korea,
and SungKyunKwan University, Suwon 440-746, Korea
[50]*Institution for Theoretical and Experimental Physics, Moscow 117259, Russia*
[51]*University College London, London WC1E 6BT, United Kingdom*
[52]*Institute of Particle Physics, University of Toronto, Toronto, Canada M5S 1A7*
(Received 8 August 2002; published 25 November 2002)

The inclusive cross section for J/ψ production times the branching ratio $B(J/\psi\rightarrow\mu^+\mu^-)$ has been measured in the forward pseudorapidity region: $B\times d\sigma[\bar{p}+p\rightarrow J/\psi(p_T>10\ \mathrm{GeV}/c, 2.1<|\eta|<2.6)+X]/\mathrm{d}\eta = 192\pm 9(\mathrm{stat})\pm 29(\mathrm{syst})$ pb. The results are based on $74.1\pm 5.2\ \mathrm{pb}^{-1}$ of data collected by the CDF Collaboration at the Fermilab Tevatron Collider. The measurements extend earlier measurements of the D0 Collaboration to higher $p_T^{J/\psi}$. In the kinematic range where the experiments partially overlap, these data are in good agreement with previous measurements.

DOI: 10.1103/PhysRevD.66.092001 PACS number(s): 13.85.Ni, 14.40.Gx

I. INTRODUCTION

The J/ψ vector meson resonance with $m=3096.87\pm 0.04$ MeV/c^2 and full width $\Gamma=87\pm 5$ keV/c^2 [1] has a 6% branching ratio into $\mu^+\mu^-$ pairs, and gives a relatively strong and clean signature at hadron colliders. The J/ψ is the lowest lying vector bound state of the $c\bar{c}$ charmonium mass spectrum. There are several channels for the appearance of a $J/\psi\rightarrow\mu^+\mu^-$ in a $\bar{p}p$ collision event. It can be produced directly, or by cascade decay of the higher mass $c\bar{c}$ states [2], resulting in a muon pair from the primary vertex. It can also be a daughter from the decay of a directly produced B meson, resulting in a muon pair from a secondary vertex because of the finite flight path of the parent B (for $B^{\pm}$ $c\tau=496$ μm [1]). These processes have been studied by the Collider Detector at Fermilab (CDF) in the central region [3], and by the D0 Collaboration in the central [4] and forward regions [5]. The study of charmonium formation in hadronic collisions is an interesting combination of perturbative and non-perturbative QCD effects. J/ψ's are useful B tags—an important decay mode for the study of CP violation is $B\rightarrow J/\psi K_s^0$. The precisely known mass and narrow width have been used to calibrate the momentum scale of spectrometers [6].

In this paper we report the measurement of inclusive J/ψ production in the forward region using the CDF magnetized iron toroids [7]. Multiple scattering in the iron broadened the narrow intrinsic width, but nevertheless the resonance produced a distinct signal in the $\mu^+\mu^-$ mass spectrum. The 7.6 m diameter toroids were located 10 m from the beam crossing, with an average acceptance polar angle of 12°. Except for the z position of the primary vertex supplied by the central CDF detector, the toroids were a stand alone instrument for measurement of the inclusive forward J/ψ cross section. In this respect this paper is distinct from other CDF publications [8].

II. DETECTOR

A. The central detector

Figure 1 shows a schematic of one-quarter of the CDF detector sectioned in the vertical plane. A pair of instrumented forward muon toroids, abbreviated by FMU, is at the far left of the figure. A more detailed view of one pair toroids is shown in Fig. 2. The entire detector was symmetric under reflection in a plane perpendicular to the colliding beams and passing through the event origin. There was an east toroid pair in the proton direction, and a west toroid pair in the antiproton direction. The CDF coordinate system z axis pointed in the proton direction, the x axis was in the horizontal plane pointing north, and the y axis was vertical pointing upwards. Polar and azimuthal angles (θ,ϕ) were defined in the conventional way, as shown in the upper left hand corner of Fig. 1. The origin was at the center of the interaction region of beam-beam collisions. The distribution of the $p\bar{p}$ collisions was Gaussian, with $\sigma=30$ cm in z, and circular in (x,y) with root mean square (rms) diameter$=40$ μm. The time between beam crossings was 3.5 μsec. Going radially outwards from the interaction region, the first detector was the silicon vertex detector (SVX) with four layers of silicon strips located between radii of 2.9 and 7.9 cm, and extending ± 25 cm in z. This instrument provided spatial measurements of charged tracks with a resolution of 13 μm in the (x,y) plane. Track finding in the SVX relied on extrapolation of tracks from the central tracking chamber (CTC).

The vertex time projection chamber (VTX), located between the SVX and the CTC, measured the primary vertex for the event based on tracking information in the (r,z) plane. The vertex used in the reconstruction of the muon pair in the toroids was based on all of the available tracking information, including the CTC, the VTX, and the SVX. At higher luminosity there was often more than one interaction per beam crossing, resulting in multiple vertices. In such cases the primary vertex was selected based on track multiplicity, transverse momentum, and other quality criteria.

There were several instrumented components to the calorimeter, both electromagnetic and hadronic, covering polar angles from 90° down to 3°. The calorimeter was segmented in azimuth $\Delta\phi$ and pseudorapidity $\Delta\eta$, where $\eta=-\log[\tan(\theta/2)]$. For the central electromagnetic, central hadronic, and wall hadronic calorimeters (CEM, CHA, and WHA) $\Delta\eta=0.1$, and $\Delta\phi=15°$. Plug electromagnetic, plug hadronic, forward electromagnetic, and forward hadronic calorimeters (PEM, PHA, FEM, and FHA) had the same $\Delta\eta$, but finer $\Delta\phi=5°$. Central and endwall calorimeters

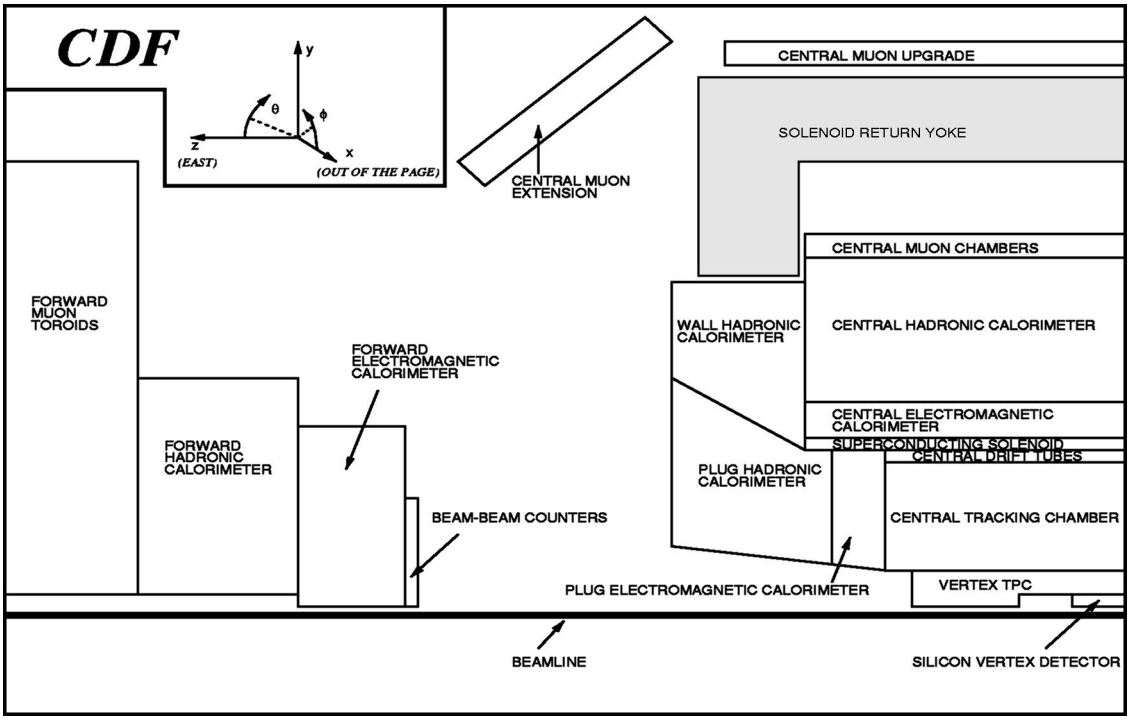

FIG. 1. Side view of one-quarter of the CDF detector. The interaction region is at the far right on the beamline. The forward muon toroids, chambers, and counters are shown schematically on the far left.

used plastic scintillator as an active sampling medium, while the plug and forward used gas proportional chambers.

B. The forward muon system

Figure 2 shows the instrumentation of the forward muon toroids. Each assembly had two iron toroids 7.6 m outer diameter, 1 m inner diameter, and 1 m thick. Each toroid was powered by four coils carrying 600 A. The average magnetic field was 1.7 T. The ratio of the rms multiple scattering angle to the bend angle for the toroid pair was 0.166. The toroid front faces were 10.13 m and 11.66 m from the CDF origin. Muon trajectories were measured with three sets of drift chambers located at 9.78 m, 11.40 m, and 13.07 m from the CDF origin. Each chamber mount consisted of two semicircular arcs split in the vertical plane and fixed to the toroid iron. The chambers were constructed in overlapping 15° wedges, and the drift cells were chords of a circle. Each chamber had two planes, the front with 56 cells, and the rear with 40 cells used to resolve ambiguities. The front plane covered pseudorapidity from 1.9 to 3.3, or polar angles from 17° to 5° with respect to each beam direction. Figure 2 shows the general pattern of drift cells in the front plane, but is not to scale. Figure 3 shows a cut away side view of the inner radius cells in the front chamber plane. The cell size increased in z to form roads which pointed to the origin, and in radius to form roads with roughly constant transverse momentum. For fixed transverse momentum, the momentum of the muon decreased with increasing radius, so the cell size grew accordingly. Each cell subtended a roughly constant pseudorapidity interval of 0.025. The longest drift time was 1 μsec. Four drift chambers in each plane, 24 in all, were outfitted with ^{55}Fe sources, which gave 6 keV Mn x rays in the 50-50 Ar-ethane chamber gas. The x-ray lines were recorded by an independent data acquisition system for daily checks on chamber gains [9]. The average single wire hit efficiency, $(97.9 \pm 0.2)\%$, was determined from the ratio (5 hit)/(6 hit) tracks $= 0.13 \pm 0.011$ for $Z \rightarrow \mu^+ \mu^-$, where the trigger muon was in the central region (see Sec. IV B). The

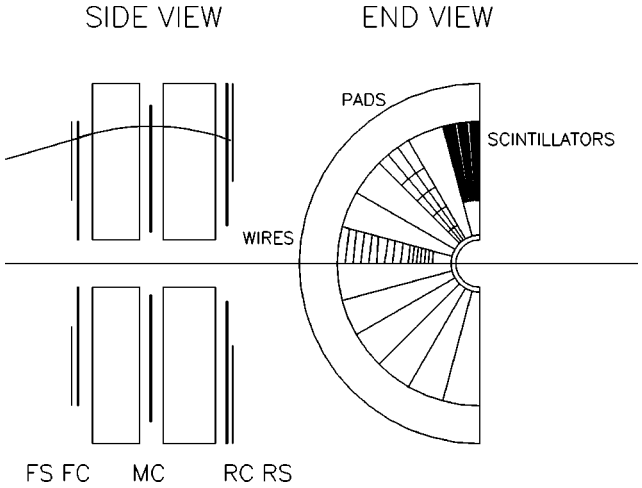

FIG. 2. Side view of one pair of toroids, showing a muon trajectory, and an end view of half of the front plane. The labels FS, FC, MC, RC, and RS in the side view refer to front scintillators, front chambers, middle chambers, rear chambers, and rear scintillators, respectively. The open boxes are the magnetized iron toroids. Going clockwise from the horizontal line in the end view, the first chamber shows the drift wires, next is the pattern of 15 cathode pads, and the top chamber shows the 5° segmented scintillators. Each 15° chamber was fully instrumented.

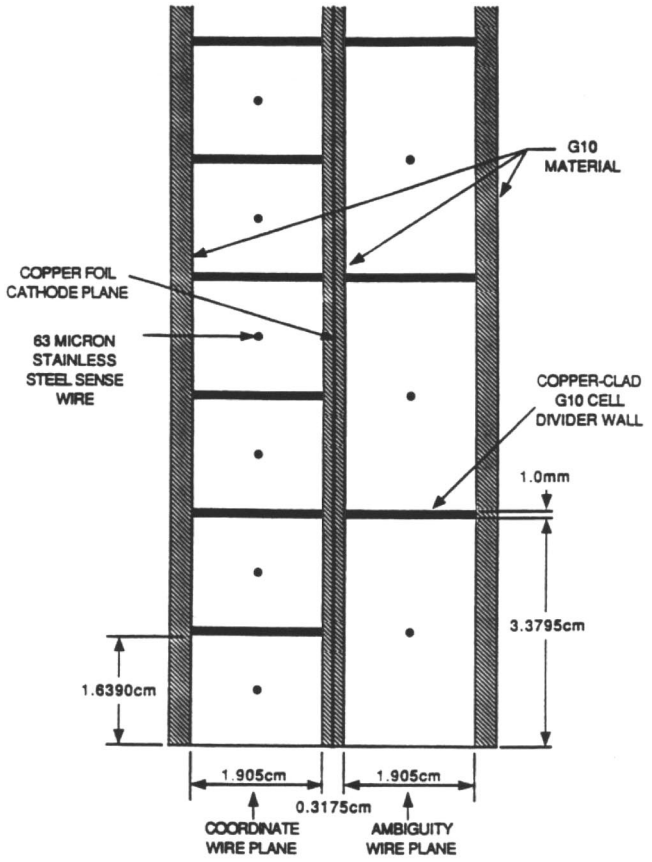

FIG. 3. Schematic side view of the front plane chamber cell geometry at the inner radius. The cell sizes increased with increasing radius to define an approximately constant p_T^μ threshold.

azimuthal angle ϕ within a wedge was measured by 15 cathode pads between the two drift cells, also shown in Fig. 2. The pads divided the wedge into three segments in ϕ each 5° wide, and five segments in η each 0.28 wide. In addition, scintillators 5° in ϕ covered pseudorapidity 1.9 to 2.8 on the front and rear chambers, but not in the middle. The scintillators were mounted on the faces of the drift chambers away from the toroid iron. The 0.5 units of pseudorapidity nearest the colliding beams did not have scintillator coverage. The effective drift chamber position resolution, including survey errors, was 650 μm. When combined with the multiple scattering, the momentum resolution was given by

$$\Delta p/p = \sqrt{(0.166)^2 + [0.0019(\mathrm{GeV}/c)^{-1}]^2 \times p^2},$$

where p is in GeV/c.

C. The forward muon trigger

A logical OR was formed of signals from three drift chamber anode wires at the same radius to create an octant in ϕ. This was done because of the low chamber hit occupancy, and the desire to limit the total number of time-to-digital converter (TDC) channels. One octant had 96 TDC channels, matched to the inputs of one FASTBUS TDC [7,11]. East and West each had 24 TDC's, for a total of 48. Commercial STRUCK latches [10] were used both to input patterns from the scintillators and pads into the data stream, and to output commands from FASTBUS to various detector components for calibration, testing, and other purposes. The pad signal amplitudes were digitized by RABBIT [12] analogue-to-digital converters (ADC's), and the scintillator signals were latched. The single muon trigger required a road through the toroids, determined by hit cells in an octant, and a matching pad and scintillator road in the same octant. The pad road was not required to overlap the drift cells in $|\eta|$ at the trigger level, but the scintillators were required to have the same 5° azimuth as the pads. The trigger was formed by picking signals off of the data readout electronics (TDC'c, ADC's, and latches), and searching for the correct patterns. Two basic cell patterns were designed to accept muons with different p_T^μ tresholds. The higher threshold road was a sequence of three cells, one in each of the front, middle, and rear chambers, which formed a tower pointing back to the origin, and was called a 1-1-1 road. The lower threshold road allowed greater bending by adding one cell above or below the pointing cell in $|\eta|$ in the middle and rear chambers, and was called a 1-3-3 road. The various patterns allowed by the logic for a 1-1-1 road, which was 50% efficient for $p_T^\mu = 7.5$ GeV/c, are described by Olsen [13]. The 1-3-3 road was 50% efficient for $p_T^\mu = 4.5$ GeV/c.

The CDF level 1 trigger accepted FMU single or dimuon triggers in coincidence with the beam-beam scintillation counters (see Sec. III). Each FMU trigger was rate limited to 0.6 Hz during data taking. This measurement employed the dimuon trigger, which used the lower threshold 1-3-3 roads. Two muon patterns were required if the muons were in different octants. For muons in the same octant, two muon drift chamber roads were required, but only one pad-scintillator coincidence. The two muons were in the same octant for about 63% of the J/ψ data sample. The rate limited level 1 dimuon trigger was automatically accepted at level 2, and passed to the on-line computer farm for level 3 analysis. Level 3 ran a version of the off-line tracking code, and accepted the event if there was a reconstructed muon pair without any p_T threshold requirement. CDF events with single or dimuon FMU triggers passing level 3 were part of the data stream sent to the offline analysis.

III. LUMINOSITY

Stable operation of the Tevatron storage ring at 900 GeV with protons and antiprotons moving in opposite directions for several hours was called a store. Two scintillator arrays, the beam-beam counters in Fig. 1, were the primary CDF luminosity monitors. The rate of hits and the total number of hits in both planes in time coincidence with beam-beam collisions were monitored during each store. The total cross section for these hits was obtained from a direct measurement of the $\bar{p}p$ elastic and total cross sections, and found to be $\sigma_{BBC} = 51.15 \pm 1.60$ mb [14]. In the 1994–1996 Tevatron collider running period, which produced the present data, the instantaneous luminosity varied from a few $\times 10^{30}$ to a few $\times 10^{31}$ cm^{-2} sec^{-1}. Since a luminosity of 5.6 $\times 10^{30}$ cm^{-2} sec^{-1} gives one count in the beam-beam counters on the average per crossing for a 51 mb cross sec-

tion and a 3.5 μsec crossing time, the total number of BBC counts had to be corrected for saturation effects. Analysis of the luminosity and data quality for this running period resulted in a file containing the integrated luminosity and average instantaneous luminosity for each of 1273 data runs [15]. Matching this list to the runs used in this J/ψ analysis gave $\int \mathcal{L}dt = 97 \pm 5$ pb^{-1}.

The 0.6 Hz rate limit restricted the FMU trigger to a fraction of the total CDF integrated luminosity. The available integrated luminosity was calculated from the trigger scalers for each run, which recorded the FMU rate before the rate limit, after the rate limit, and the number of rate limited triggers. The efficiency for the FMU dimuon trigger averaged over the entire data sample was $\epsilon_{trig} = 0.765 \pm 0.040$, giving an available luminosity of $\int \mathcal{L}dt = 74.2 \pm 5.2$ pb^{-1}.

IV. DATA SELECTION

A. Event reconstruction

The off-line code reconstructed the entire CDF event, with tracking, vertex, calorimetry, and muons. The primary vertex was a parameter in the FMU fit to a muon trajectory. As mentioned in the description of the central detector, high luminosity could give multiple vertices, which could lead to ambiguity in choosing the correct vertex. The rate limit applied to the FMU trigger tended to weight the data sample towards lower luminosity, where this problem was minimized. In addition, because of the small polar angle of the toroids, any vertex error made only a minor contribution to the mass resolution, which was dominated by multiple scattering in the iron and position measurement errors in the FMU drift chambers.

The FMU reconstruction package searched for muons in both sets of toroids for every event. After converting wire hit drift times to distances, and resolving the ambiguities, a vertex constrained parabolic fit to the trajectory of the form:

$$r(z) = r_0 + z \times \tan(\theta_0) + k \times (z - z')^2,$$

where z' was the front face of the first toroid. The gap between toroids was ignored in this first pass fit. The constant r_0 was the intercept at the origin due to the displaced vertex, θ_0 was the initial polar angle of the track, and the parameter k, fitted from the front face of the first toroid through the rear face of the second toroid, was inversely proportional to the momentum. The momentum obtained from this fit was then used to refit the track taking into account multiple scattering and energy loss in the calorimeters and toroids [16]. A χ^2 was obtained for each fitted track. The trigger was not required for track reconstruction.

Regarding other tracking information from the CDF Central Detector, while there was some geometrical overlap between the coverage of the SVX and the FMU, particularly for vertices shifted away from the toroids, it was not possible to identify the appropriate SVX tracks because of the wide road necessary to accommodate the multiple scattering in the calorimeters in extrapolating the toroid tracks back to the vertex. As a result, the good spatial resolution of the SVX could not be exploited to determine whether the $\mu^+\mu^-$ pair originated at a primary or secondary vertex, which would separate prompt J/ψ's from B daughters. There was no useful geometrical overlap between the forward toroids and the CTC. Jet activity was measured for each event by the calorimeters. About 60% of the final muon pair data sample had at least one jet with transverse energy above 10 GeV. The majority of the jet activity balanced the $p_T^{\mu^+\mu^-}$ of the muon pair, without further illuminating the event topology.

The fit program allowed several user input parameters, such as the number of hits on the track (6), whether the vertex constraint was used or not (yes), the cell width of the search road (1-3-3), and the width of the road in azimuth (5°). The off-line created cassette tapes with complete CDF events which had at least one reconstructed FMU. A file containing all events with more than one forward muon was created from these tapes.

B. Selection criteria

Figure 4 shows the opposite sign pair mass distribution in the FMU dimuon data sample after event reconstruction. A broad peak in the dimuon invariant mass at around 3 GeV/c^2 is apparent in the top plot, and becomes clearer after the subtraction of the like sign background. The like sign background was almost half the total at this stage, but was only 5% after the quality selection criteria, which had little effect on the peak signal. The following selection criteria were applied to this data sample:

(1) Total number of hits in the octant fewer than 40.
(2) $\mu^+\mu^-$ pair mass between 1 and 6 GeV/c^2.
(3) Opening angle cut $\Delta\phi > 0.1$ or $\Delta\eta > 5$ cells (approximately 0.16 units).
(4) $p_T^{\mu^+\mu^-} > 10$ GeV/c.
(5) $\chi^2 < 11.6$ for each track, ideal χ^2 probability $> 98\%$.
(6) $p_T^{\mu 1} > 5$ GeV/c and $p_T^{\mu 2} > 2$ GeV/c.
(7) Opposite charge $\mu^+\mu^-$ pair.
(8) $2.1 < |\eta^{\mu^+\mu^-}| < 2.6$.
(9) Two FMU level 3 trigger.

The first criterion eliminated events where the number of background hits in the octant was greater than 28 for two six hit tracks. The effect of this requirement has been studied by Olsen [13]. For the present data sample its efficiency was $(90 \pm 5)\%$. The next two requirements eliminated the very low mass peak. Background contributions to the small opening angle region came from extra hits by delta rays off a real track which could fake a second muon. The toroids, placed 10 m from the event origin, had poor efficiency for detection in the higher mass region, around the Υ. The J/ψ fell in the mass range where the detection efficiency for high $p_T^{\mu^+\mu^-}$ pairs was favorable. In the 1–6 GeV/c^2 mass window, the efficiency dropped off sharply for $p_T^{\mu^+\mu^-} < 10$ GeV/c, because of the limited solid angle of FMU, as shown in Fig. 5, which has all of the listed criteria except No. 4. The $\chi^2 < 11.6$ cut on each track removed $10 \pm 2\%$ of the tracks, instead of the 2% expected for a classic χ^2 distribution. See Fig. 6. The various errors in track reconstruction from multiple scattering, wire position errors, and extra hits were reproduced by the detector simulation Monte Carlo. The simu-

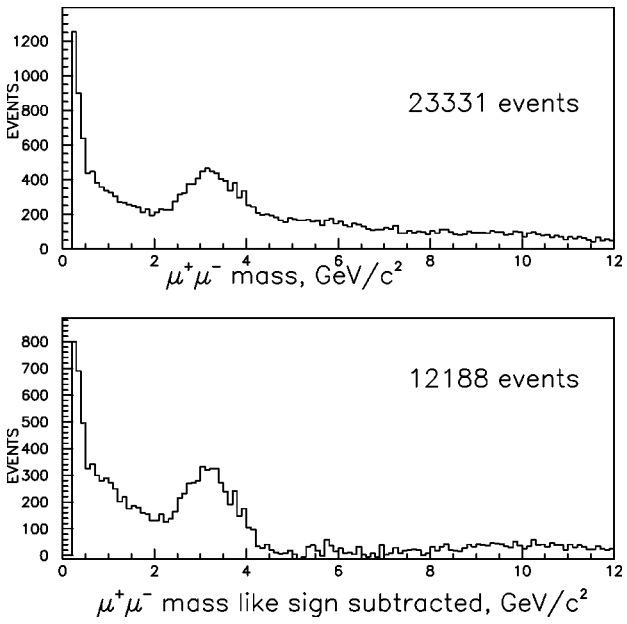

FIG. 4. Opposite sign pair mass distributions from the reconstructed data file, before (top), and after (bottom) like sign subtraction.

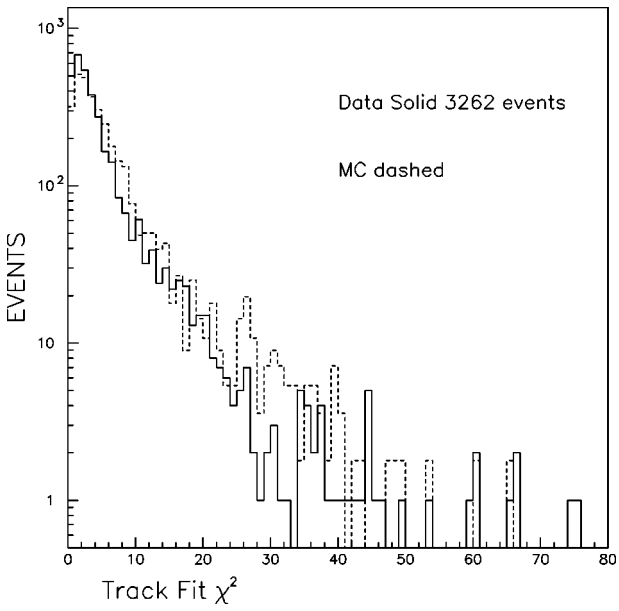

FIG. 6. χ^2 distribution for the single muon track fit compared to Monte Carlo.

lated χ^2 distribution, also shown in Fig. 6, had $15\pm3\%$ above $\chi^2=11.6$. The individual muon p_T^μ requirements, where the first muon was the one with higher p_T^μ, were made to retain good trigger efficiency. The requirements on $|\eta|$ eliminated regions 0.1 unit wide at the detector boundaries, and gave an overall $\Delta\eta=1$ for the measurement.

The two FMU level 3 trigger efficiency depended on several factors. Relative efficiencies of the drift chambers were monitored using the Fe sources as described above. For a six hit track, the wire hit efficiency was $\epsilon_{wire}=(0.98)^6=0.88\pm0.03$. The total single muon trigger efficiency was measured using a sample of 1100 $Z^0\rightarrow\mu^+\mu^-$ decays, where the CDF detector was triggered by the high p_T^μ central muon. Whether or not the event was also triggered by the forward muon was recorded. If the reconstructed FMU satisfied the trigger requirements, but failed to trigger, it was called an inefficiency [17]. The trigger efficiency calculated from the number of failures was $71.4\pm1.6\%$. Since this number was the product of the efficiencies of the wires, pads, and scintillators, the scintillator-pad coincidence efficiency was 0.81 ± 0.04. As described above in the section on the forward muon trigger, the dimuon trigger required one pad-

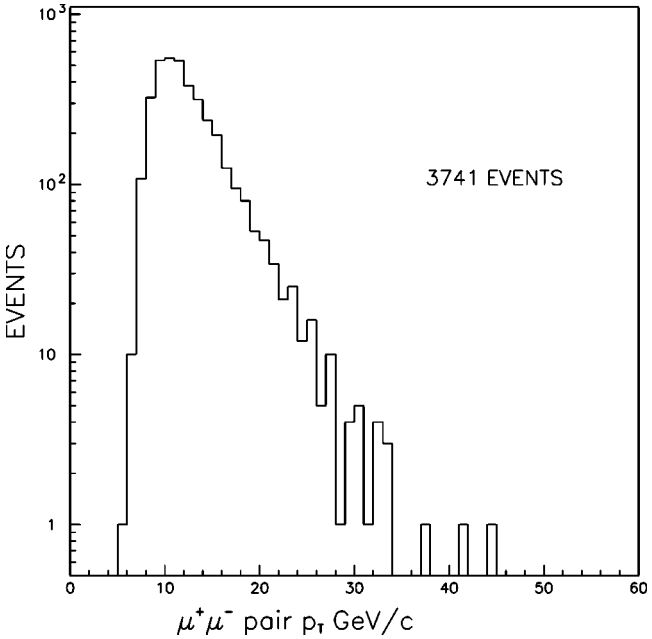

FIG. 5. Opposite sign $p_T^{\mu^+\mu^-}$ distribution.

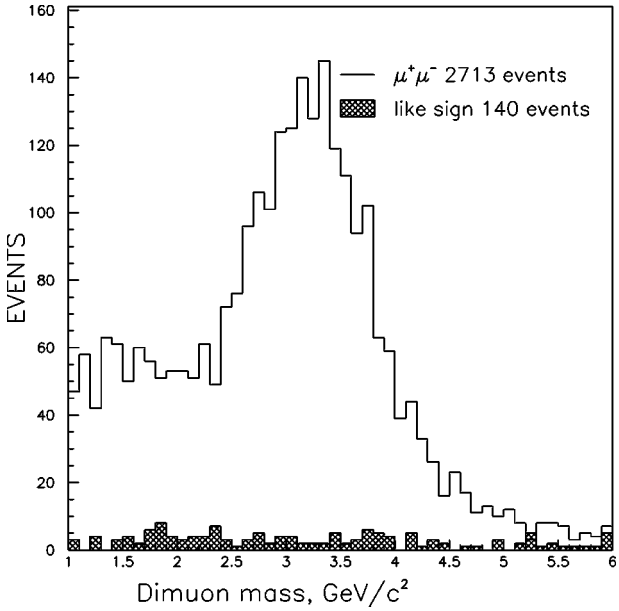

FIG. 7. Data mass plot after all cuts. The like sign data are plotted separately.

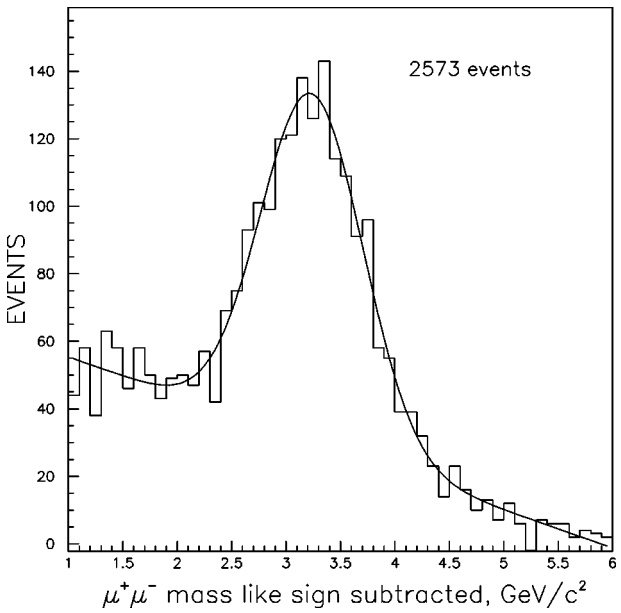

FIG. 8. Final data sample after like sign subtraction. The Gaussian peak is at 3.23 ± 0.02 GeV/c^2, with $\sigma=0.47\pm0.02$ GeV/c^2. The overall fit $\chi^2=50$ for 45 degrees of freedom.

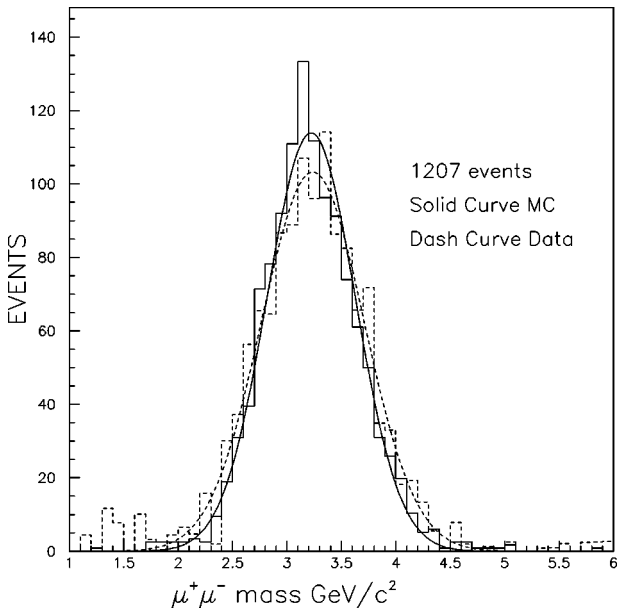

FIG. 9. Background subtracted data compared to the J/ψ Monte Carlo. The MC peak is at 3.22 ± 0.01 GeV/c^2, with $\sigma=0.41\pm0.01$ GeV/c^2. The Gaussian fit to the data is the same as Fig. 8: peak at 3.23 ± 0.02 GeV/c^2 and $\sigma=0.47\pm0.02$ GeV/c^2.

scintillator road for both muons in the same octant, but two independent single muon triggers if the muons were in different octants. Thus the trigger efficiency depended on the same octant vs different octant mix. Relaxing the two FMU trigger requirement resulted in a 25% increase in the data sample. Every event was a single muon trigger. This increase was consistent with expectations from the single muon trigger efficiency, and therefore required no further corrections. All quality criteria were applied to the dimuon Monte Carlo discussed below in deriving the detector acceptance.

C. Data and Monte Carlo

The mass plot after all quality requirements is shown in Fig. 7, together with the like sign data. The opposite sign plot after like sign background subtraction is shown in Fig. 8. The like sign subtraction was assumed to eliminate backgrounds from uncorrelated muons from π or K decays in flight. There are 2573 events in the final mass plot, which was fitted to a linear background plus a Gaussian signal. The full mass window from 1 GeV/c^2 to 6 GeV/c^2 was used to fit the background shape underneath the peak. The peak after background subtraction is shown in Fig. 9. There were 1207 events in this peak between $2.0<M(\mu^+\mu^-)<4.4$ GeV/c^2, a window centered at 3.2 GeV/c^2, and 2.5σ wide. The fitted background in this same mass window was 730 events, for a signal fraction of $62\pm2\%$, where the uncertainty is statistical.

In order to evaluate the systematic uncertainty associated with this procedure, the dependence of this fraction on the assumed shape of the background was studied. Two other background functions were used to compare with the linear one above. The results are summarized in Table I. One was a simple exponential, which gave a larger signal fraction, with a slightly wider Gaussian peak and a slightly larger χ^2. The second background model used templates calculated from three sources of dimuon background: Drell-Yan muon pairs [18], muon pairs from sequential decays of B and D mesons, and a small tail from a ϕ peak at 1 GeV/c^2 [8]. The relative normalizations of the templates were allowed to float, as was the amount of Gaussian signal. This procedure resulted in a yield halfway between the other two, with a good χ^2. The average of the linear and exponential signal fractions was adopted for the cross section calculation. A systematic uncertainty of 7.9% was assigned to account for the dependence on the assumed background shape. The $p_T^{J/\psi}$ dependence of this fraction is given in Table II. The systematic uncertainties in the three highest p_T bins were larger than the 7.9% applied to the data sample as a whole, and those uncertainties have

TABLE I. Signal and background in $2<M(\mu^+,\mu^-)<4.4$ GeV/c^2 for various background functions. In columns six and seven DOF refers to the number of fitted points minus the number of parameters.

Fit type	Signal	Background	s	peak σ GeV/c^2	d.o.f	χ^2/DOF
linear	1206	731	0.62 ± 0.02	0.47 ± 0.01	45	1.11
exponential	1397	540	0.72 ± 0.02	0.51 ± 0.01	45	1.33
templates	1294	643	0.67 ± 0.02	0.48 ± 0.01	41	0.73

TABLE II. $p_T^{J/\psi}$ dependent corrections to the data, with statistical uncertainties.

$p_T^{\mu^+\mu^-}$ (GeV/c)	Data	s	MC general	MC accepted	ϵ_{MC}
10–15	1379±38	0.69±0.020	12500	1287	0.103±0.0035
15–20	411±21	0.65±0.034	1920	498	0.259±0.011
20–25	106±10	0.71±0.092	350	136	0.388±0.029
25–30	29±5.6	0.59±0.16	83	38	0.46±0.055
30–35	10±3	0.59±0.27	18	6	0.33±0.11

been added in quadrature with the statistical uncertainties in column 3 of Table II.

The Monte Carlo peak is compared to the data from the linear background fit in Fig. 9. The peak shift from 3.1 GeV/c^2 to 3.2 GeV/c^2 was reproduced by the Monte Carlo simulation. This effect was caused by a combination of the opening angle requirement, and the tendency for the reconstructed momentum to be a few percent high. The $\psi(2S)$ at 3.7 GeV/c^2 could contribute to this shift, but was expected to be only about 2% of the J/ψ's, and hence undetectable [3]. The Monte Carlo width of 0.41 GeV/c^2 was slightly narrower than the experimental width of 0.47 GeV/c^2, but the agreement was on the whole satisfactory. The experimental width depended slightly on the assumed shape of the background (see Table I). The signal fraction systematic uncertainty in Table III was increased to allow for the width discrepancy between data and the Monte Carlo calculation.

The detector acceptance for $J/\psi \to \mu^+\mu^-$ was a function of three independent variables: p_T and η of the J/ψ, and the muon angular distribution in the J/ψ rest frame. The acceptance was calculated using a Monte Carlo calculation which generated $B \to J/\psi + X$. This channel for J/ψ production was chosen for simplicity, and the resulting kinematic distributions adequately modeled the data for acceptance calculations. However, B decays were only one of the possible sources of J/ψ's in the data, which included prompt J/ψ's and daughters from χ decays as well. The Monte Carlo calculation started with a p_T^B distribution patterned after CDF central data [3]. The B rapidity was chosen independent of p_T^B to be flat for $|y|<2$, and to drop off linearly to zero from $|y|=2$ to $|y|=4$. The J/ψ momentum in the B rest frame was generated isotropically according to the measured inclusive spectrum from B decays [19]. The resulting $p_T^{J/\psi}$ distribution was reweighted to agree with the distribution measured by D0 [5] in the bins 5 GeV/c $<p_T<$ 15 GeV/c, around the cut at 10 GeV/c, to assure that the momentum resolution effect on the spectrum was correctly modeled. The resulting MC accepted p_T distribution in column 5 of Table II agreed closely with the data in column 2 of the same table. The J/ψ η distribution decreased linearly by a factor of two from $|\eta|=2$ to $|\eta|=3$, across the acceptance of the toroids. After all quality criteria were applied, the Monte Carlo sample η distribution agreed with the data within the statistical uncertainty. This $|\eta|$ dependence was also consistent with the results shown in Fig. 10. The muon pairs were generated isotropically in the J/ψ rest frame. The sensitivity of the acceptance to non-isotropic pair distributions was studied by choosing the J/ψ line of flight to be the quantization axis for its spin vector, and comparing $m_s=\pm 1$, $f(\theta)=3[1+\cos^2(\theta)]/8$, to $m_s=0$, $f(\theta)=3[1-\cos^2(\theta)]/4$. The result was $[N(m_s=0)-N(m_s=\pm 1)]/[N(m_s=0)+N(m_s=\pm 1)] = (8\pm 2)\%$. The $m_s=0$ distribution favored symmetric muons with larger opening angles, and therefore had a larger acceptance. Since the mix of $m_s=\pm 1$ and $m_s=0$ in the data was unknown, the systematic uncertainty for the Monte Carlo efficiency included this effect (see row 4 of Table III).

The muons so obtained were subjected to a detector simulation program which included ionization energy loss dE/dx and multiple scattering in the iron of the calorimeters and the toroids, deflection in the magnetized iron, a small deflection in the solenoid field, errors in the vertex location, chamber wire efficiency, extra hits from delta rays, wire position errors, and drift chamber resolution. The resulting track patterns were then required to satisfy the trigger. As shown in

TABLE III. Systematic uncertainties.

Source	Factor	Uncertainty
$\int \mathcal{L} dt$	74.0±5.2 pb^{-1}	7.0%
Signal fraction	0.68±0.054	7.9%
Monte Carlo efficiency	0.132±0.011	8.3%
Trigger efficiency	0.74±0.05	6.7%
	Total systematic uncertainty	15.0%

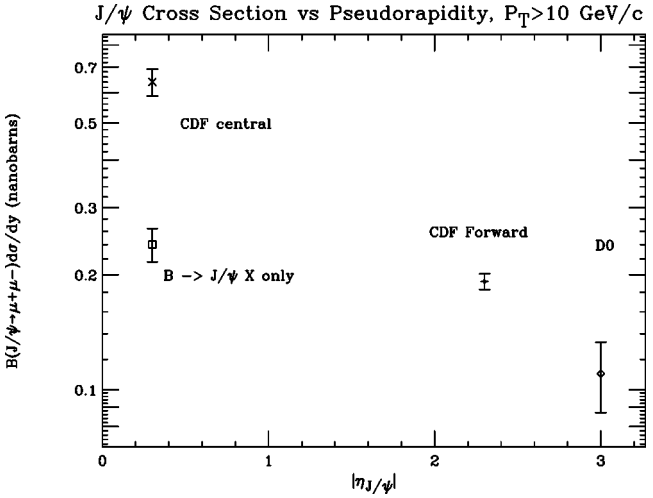

FIG. 10. Integrated CDF and D0 cross sections vs $|\eta|$ for $p_T^{J/\psi} > 10$ GeV/c. The uncertainties shown are statistical only.

TABLE IV. $p_T^{J/\psi}$ dependent cross sections. Uncertainties are statistical only. The factor B is the branching ratio for $J/\psi \to \mu^+\mu^-$.

$p_T^{J/\psi}$ (GeV/c)	Data$\times s/(\epsilon_{MC})$	$B\times d\sigma/dp_T d\eta$ (pb/GeV/c)
10–15	9238±480	33.7±1.8
15–20	1031±87	3.80±0.32
20–25	194±35	0.71±0.13
25–30	37±13	0.135±0.047
30–35	18±11	0.066±0.040

Figs. 6 and 9, the detector simulation adequately modeled the data.

V. RESULTS

Table II begins the calculation of the $p_T^{\mu^+\mu^-}$ dependent cross section, which is completed in Table IV. The data listed in column 2 of Table II are the numbers of events in the $2.0<M(\mu^+\mu^-)<4.4$ GeV/c^2 mass range, after subtraction of the like sign background. There were no events in the 35–40 GeV/c bin, and two events with $p_T^{\mu^+\mu^-}>40$ GeV/c. The quoted statistical uncertainty was calculated from the number before the like sign subtraction. Column 3 is the bin by bin calculation of the peak fraction in the $2.0<M(\mu^+\mu^-)<4.4$ GeV/c^2 mass range. The detection efficiency was calculated by dividing the number of events generated by the Monte Carlo calculation (column 4) by the number which passed all cuts (column 5), as a function of reconstructed $p_T^{J/\psi}$. The uncertainties listed in columns 3 and 6, when combined in quadrature with those in the data in column 2, gave the statistical uncertainties to the corrected data in column 2 of Table IV. The systematic uncertainty in the signal fraction was dominated by the lower momentum bins, and is applied to the cross section as shown in Table III. Table IV also shows the resulting cross sections with statistical uncertainties. The multiplier to get from column 2 to column 3 of Table IV was

$$f = 1 \Big/ \left(\int \mathcal{L}dt \times \Delta p_T \times \varepsilon \right) = 0.00365 \pm 0.00033(\text{syst})\ \text{pb/GeV}/c.$$

The normalization factors in this expression are as follows:

(1) $\int \mathcal{L}dt = 74.2 \pm 5.2\ \text{pb}^{-1}$.

(2) $\Delta p_T^{\mu^+\mu^-} = 5$ GeV/c.

(3) $\varepsilon = 0.74 \pm 0.05$ is the trigger and cut efficiency factor not in the Monte Carlo.

The uncertainties in f were systematic, and are listed in Table III. The cross section integrated over $p_T^{J/\psi}$ was calculated by summing the data in column 2 of Table IV, and multiplying by $f \times \Delta p_T^{\mu^+\mu^-}$. The result, including statistical and systematic uncertainties, was

$$B(J/\psi \to \mu^+\mu^-) \times d\sigma[\bar{p} + p \to J/\psi(p_T > 10\ \text{GeV}/c, 2.1<|\eta|<2.6) + X]/d\eta = 192 \pm 9(\text{stat}) \pm 29(\text{sys})\ \text{pb}.$$

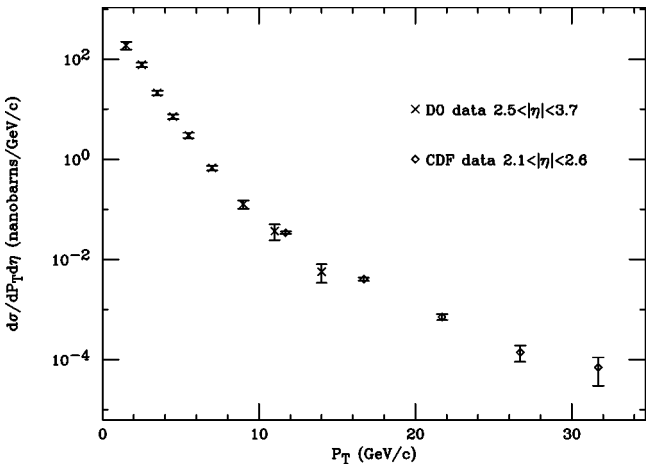

FIG. 11. CDF and D0 forward cross sections vs $p_T^{J/\psi}$. The average pseudorapidity for CDF $\langle|\eta|\rangle = 2.3$, while for D0 $\langle|\eta|\rangle = 3$. The uncertainties shown are statistical only. The CDF data points also have a common systematic uncertainty of ±15%.

VI. CONCLUSIONS

The cross sections from Table IV are plotted together with the D0 results [5] in Fig. 11. The two experiments have different average pseudorapidities: CDF $\langle|\eta|\rangle = 2.3$ and D0 $\langle|\eta|\rangle = 3$. The agreement between the two experiments in the p_T region where they overlap is satisfactory. The CDF measurements increase the maximum $p_T^{J/\psi}$ by a factor of two. Over this range the cross section drops an order of magnitude. The CDF integrated cross section $d\sigma/d\eta$ for $p_T > 10$ GeV/c was $B(J/\psi \to \mu^+\mu^-)d\sigma[\bar{p} + p \to J/\psi(p_T > 10\ \text{GeV}/c, 2.1<|\eta|<2.6) + X]/d\eta = 192 \pm 9(\text{stat}) \pm 29(\text{syst})$ pb.

Figure 10 shows integrated cross sections in different $|\eta|$ regions for $p_T^{J/\psi} > 10$ GeV/c. The points were obtained by integrating the published cross sections for CDF central [3], and D0 forward [5]. CDF in the central rapidity region separated the prompt J/ψ's from the J/ψ daughters from B meson decay using the secondary vertex distribution measured in the SVX, and this data point is also shown for $p_T^{J/\psi} > 10$ GeV/c. A similar separation for the forward data set was not possible.

ACKNOWLEDGMENTS

We thank the Fermilab staff and the technical staffs of the participating institutions for their vital contributions. This work was supported by the U.S. Department of Energy and the National Science Foundation; the Italian Istituto Nazionale di Fisica Nucleare; the Ministry of Education, Science and Culture of Japan; the Natural Sciences and Engineering Research Council of Canada; the National Science Council of the Republic of China; the Swiss National Science Foundation; the A.P. Sloan Foundation; the Bundesministerium fuer Bildung und Forschung, Germany; the Korea Science and Engineering Foundation (KoSEF); the Korea Research Foundation; and the Comision Interministerial de Ciencia y Tecnologia, Spain.

[1] Particle Data Group, D. Groom *et al.*, Eur. Phys. J. C **15**, 1 (2000).
[2] P. Cho and A. Leibovich, Phys. Rev. D **53**, 150 (1996); **53**, 6203 (1996).
[3] CDF Collaboration, F. Abe *et al.*, Phys. Rev. Lett. **79**, 572 (1997); **79**, 578 (1997).
[4] D0 Collaboration, S. Abachi *et al.*, Phys. Lett. B **370**, 239 (1996).
[5] D0 Collaboration, B. Abbott *et al.*, Phys. Rev. Lett. **82**, 35 (1999).
[6] CDF Collaboration, F. Abe *et al.*, Phys. Rev. D **52**, 4784 (1995).
[7] K. Byrum *et al.*, Nucl. Instrum. Methods Phys. Res. A **268**, 46 (1988).
[8] A detailed account of this analysis is in J. Steele, Ph.D. dissertation, University of Wisconsin, Madison, 2000.
[9] L. Markosky, Ph.D. dissertation, University of Wisconsin, Madison, 1992.
[10] STR136 latch manufactured by Struck Innovative Systems, Hamburg, Germany.
[11] E. Barsotti *et al.*, Nucl. Instrum. Methods Phys. Res. A **269**, 82 (1988).
[12] G. Drake *et al.*, Nucl. Instrum. Methods Phys. Res. A **269**, 68 (1988).
[13] J. Olsen, Ph.D. dissertation, University of Wisconsin, Madison, 1998.
[14] CDF Collaboration, F. Abe *et al.*, Phys. Rev. Lett. **76**, 3070 (1996).
[15] The CDF luminosity analysis is described by D. Cronin-Hennessy, A. Beretvas, and P.F. Derwent, Nucl. Instrum. Methods Phys. Res. A **443**, 37 (2000).
[16] P. Billoir, Nucl. Instrum. Methods Phys. Res. A **225**, 353 (1984); P. Billoir, R. Fruhwirth, and M. Regler, *ibid.* **241**, 115 (1985); for a description of the application to the FMU toroids, see J. Skarha, Ph.D. dissertation, University of Wisconsin, Madison, 1989.
[17] CDF Collaboration, F. Abe *et al.*, Phys. Rev. D **61**, 032001 (2000).
[18] The authors are grateful to D. Zeppenfeld for the use of a next to leading order Drell-Yan Monte Carlo program.
[19] R. Balest *et al.*, Phys. Rev. D **52**, 2661 (1995).